

Catalytic role of in-situ formed C-N species for enhanced Li_2CO_3 decomposition

Received: 25 August 2023

Accepted: 8 April 2024

Published online: 22 April 2024

Check for updates

Fangli Zhang^{1,2,3}, Wenchao Zhang^{1,4}✉, Jodie A. Yuwono², David Wexler³, Yameng Fan³, Jinshuo Zou², Gemeng Liang², Liang Sun² & Zaiping Guo²✉

Sluggish kinetics of the CO_2 reduction/evolution reactions lead to the accumulation of Li_2CO_3 residuals and thus possible catalyst deactivation, which hinders the long-term cycling stability of Li- CO_2 batteries. Apart from catalyst design, constructing a fluorinated solid-electrolyte interphase is a conventional strategy to minimize parasitic reactions and prolong cycle life. However, the catalytic effects of solid-electrolyte interphase components have been overlooked and remain unclear. Herein, we systematically regulate the compositions of solid-electrolyte interphase via tuning electrolyte solvation structures, anion coordination, and binding free energy between Li ion and anion. The cells exhibit distinct improvement in cycling performance with increasing content of C-N species in solid-electrolyte interphase layers. The enhancement originates from a catalytic effect towards accelerating the Li_2CO_3 formation/decomposition kinetics. Theoretical analysis reveals that C-N species provide strong adsorption sites and promote charge transfer from interface to $^*\text{CO}_2^{2-}$ during discharge, and from Li_2CO_3 to C-N species during charge, thereby building a bidirectional fast-reacting bridge for CO_2 reduction/evolution reactions. This finding enables us to design a C-N rich solid-electrolyte interphase via dual-salt electrolytes, improving cycle life of Li- CO_2 batteries to twice that using traditional electrolytes. Our work provides an insight into interfacial design by tuning of catalytic properties towards CO_2 reduction/evolution reactions.

Severe global warming has resulted in pledges by current society to achieve the goals of carbon neutrality with projections of atmospheric carbon peaking followed by eventual falls¹⁻³. In this context, how to achieve eco-efficient and environmentally sustainable CO_2 capture, and to reconstruct energy device systems for balancing reduction of carbon emissions and growing energy demands has become a worldwide challenge^{4,5}. Rechargeable Li- CO_2 batteries are considered potential candidates for advanced energy storage devices and CO_2 fixation. There is potential to achieve a win-win situation due to their relatively high discharge potential (2.80 V vs. Li^+/Li) and theoretical

specific energy density (1876 Wh kg^{-1}), based on the reversible redox reaction of $3\text{CO}_2 + 4\text{Li}^+ + 4\text{e}^- \leftrightarrow 2\text{Li}_2\text{CO}_3 + \text{C}^{6,7}$. In the field of space exploration, it has been projected by NASA that uptake of Li- CO_2 batteries would enable significant weight and cost savings for Mars exploration missions because 96% of the Martian atmosphere is CO_2 ^{8,9}. In both these areas, Li- CO_2 batteries represent potentially attractive options.

The sluggish kinetics of CO_2 reduction/evolution reactions (CRR/CER) and the poor charge transfer capability of Li- CO_2 batteries generally lead to the accumulation of Li_2CO_3 residuals and high charge

¹School of Metallurgy and Environment, Central South University, Changsha 410083, China. ²School of Chemical Engineering, The University of Adelaide, Adelaide, SA 5005, Australia. ³Institute for Superconducting & Electronic Materials, University of Wollongong, Faculty of Engineering and Information Science, Wollongong, NSW 2500, Australia. ⁴Chinese National Engineering Research Centre for Control & Treatment of Heavy Metal Pollution, Changsha 410083, China. ✉e-mail: wenchao.zhang@csu.edu.cn; zaiping.guo@adelaide.edu.au

potential, which further results in fast electrolyte degradation and consequent deterioration in battery cyclability^{10,11}. Electrolyte engineering has been regarded as an effective and practical approach to addressing limited battery performance^{12–14}. In the past, tremendous efforts have been dedicated to constructing robust inorganic-rich solid-electrolyte interphase (SEI) layers on electrodes, especially fluorinated SEIs, to suppress parasitic reactions between electrodes and electrolytes and improve battery cyclability^{15–19}. Indeed, the organic components in the SEI layer have been considered to possess porous structures, which leads to an increase in the SEI thickness and exacerbates the non-uniform diffusion of Li⁺ ions at the interface^{16,20}. However, detailed reaction mechanisms of the organic SEI components (e.g., C-N, C-F, C-S, etc.) and their catalytic effects have barely been studied in the past few decades, particularly in relationship to CO₂ reduction/evolution chemistry. Furthermore, how to achieve a fundamental understanding of the key roles of organic SEI components in determining reaction kinetics and reversibility of Li₂CO₃, and, finally, governing battery performance has remained a mystery for decades. Therefore, it is of great importance to initiate investigation of the organic components in SEIs with the hope of revealing their structures and corresponding features, including their formation mechanism, adsorption of the reactant gas CO₂, intermediate *CO₂²⁻ radicals, and the discharge product Li₂CO₃, and corresponding catalytic activity.

Herein, we have initiated fundamental studies of the organic components in SEI layers and attempted to decipher the mysteries associated with their electrochemical performance in Li-CO₂ batteries. To better explore and detect the catalytic effects of SEI components, reduced graphene oxide (rGO) with poor catalytic performance was employed as a matrix on cathodes. Among the several traditional single-salt-based electrolytes, even with lower content of LiF in the SEI layer compared to that in lithium bis(trifluoromethanesulfonyl)imide (LiTFSI)-based electrolyte, the cells in lithium bis(fluorosulfonyl)imide (LiFSI)-based electrolyte containing a higher content of C-N species in the SEI layer could deliver relatively longer cycle life. Characterizations of cycled cathodes confirm that the content of C-N species is tightly

correlated with reversibility of Li₂CO₃, which is the key to determining the battery cycling. First-principles calculation results show that C-N species at the interface can provide strong adsorption sites and fast charge transfer capability to *CO₂²⁻ and Li₂CO₃, which can enhance the interfacial catalytic properties to accelerate the CRR/CER kinetics. In the CRR, spontaneous charge transfer can be achieved between C-N species and *CO₂²⁻, which could drive the *CO₂²⁻ to quickly react with C₂O₄²⁻ to generate CO₃²⁻, thus facilitating the formation of Li₂CO₃. In the CER, the strong interaction between Li atoms in Li₂CO₃ and the interfacial N sites of C-N species enable fast charge transfer from Li₂CO₃ to C-N species, which can notably weaken Li-O bonds in Li₂CO₃ and decrease its decomposition energy barriers. When paired with a ruthenium (Ru) catalyst, the Li-CO₂ cells also follow the same tendency as above, indicating that the positive effects of C-N species towards battery cycling are applicable with the participation of a metal catalyst. To further improve battery cycling by increasing the content of C-N species, a C-N rich SEI layer was constructed in dual-salt (LiNO₃/LiFSI)-based electrolytes. With this SEI layer, cells in 0.25 M LiNO₃/0.75 M LiFSI electrolytes could achieve stable long-term cycling of >1500 h with a metal-free catalyst of rGO and prolonged cycling of >2200 h with an Ru catalyst. Our finding opens an avenue to address the bottleneck issue for Li-CO₂ batteries and provides an electrolyte design principle for guiding future electrolyte design in batteries.

Results

Modelling for adsorption energy and charge transfer analyses

The CO₂ reduction/evolution reactions are relatively complicated processes in Li-CO₂ batteries, occurring through multiple intermediate steps, as shown in Equations S(1)-(4) and Supplementary Fig. 1 in the Supplementary Information^{21,22}. On the one hand, *CO₂²⁻, as a key intermediate radical, is a crucial driving force that governs spontaneous charge transfer capability and reduces the formation energy barrier of Li₂CO₃, both of which dominate the CO₂ reaction kinetics (Fig. 1a). On the other hand, the lifespan of Li-CO₂ batteries is determined by the reversibility of the discharge product Li₂CO₃, due to its insulating nature²³. To unveil the relationship between the CO₂

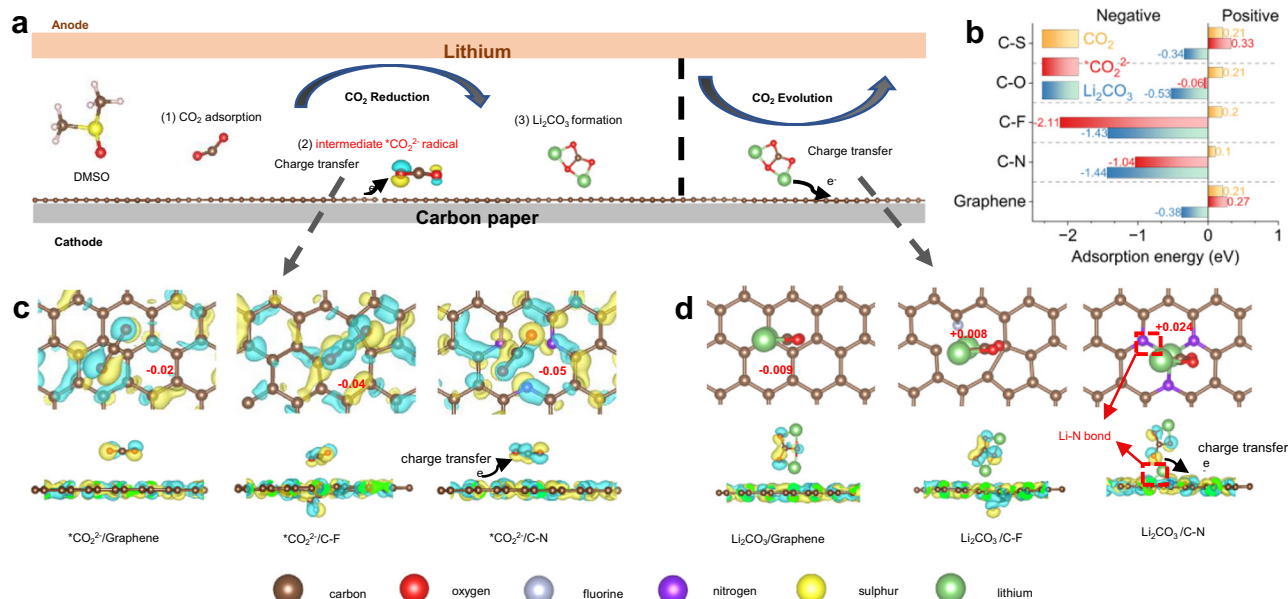


Fig. 1 | Modelling for adsorption energy and charge transfer analyses of various SEI compositions. **a** Schematic representation of the CO₂ reduction/evolution processes on the cathode surfaces. **b** Adsorption energies of graphene, C-N, C-F, C-O, and C-S species for CO₂, *CO₂²⁻, and Li₂CO₃. Top views and side views of the atomic structures and the charge density differences of **(c)** *CO₂²⁻ and **(d)** Li₂CO₃ adsorption on graphene, C-F, and C-N species. The red numbers are the Bader

charge values of these different species for *CO₂²⁻ and Li₂CO₃ molecules. The yellow and blue zones represent electron loss and gain, respectively (isovalue, 2 × 10⁻⁶). The carbon, oxygen, fluorine, nitrogen, sulphur, and lithium atoms are marked as copper, red, silver, purple, yellow, and light green, respectively.

reaction kinetics and the cathode surface chemistry, we first constructed bonding configurations for basic graphene and common organic SEI components (Supplementary Fig. 2) and compared their adsorption energy for CO_2 , $^*\text{CO}_2^-$, and Li_2CO_3 by first-principles calculations to systematically investigate their configurations and catalytic properties (Supplementary Table 1).

In the CRR, C-N species show relatively higher adsorption energies towards CO_2 (0.1 eV) and $^*\text{CO}_2^-$ (−1.04 eV) than C-O, C-S, and graphene (Fig. 1b, yellow and red bars, respectively), indicating a lower formation barrier of Li_2CO_3 and higher catalytic activation on C-N species. After adsorption, the charge transfer capabilities determined by the interaction between $^*\text{CO}_2^-$ and the electrode surface layer are critical to governing the reaction kinetics. Therefore, as typical examples, Bader charge and charge density difference analyses for graphene, C-N, and C-F species were conducted to comprehensively study their charge transfer capability. As presented in Fig. 1c, the value of spontaneous charge transfer is the largest from C-N species to $^*\text{CO}_2^-$ (−0.05 e^-), whereas its value on graphene and C-F species is smaller (around −0.02 and −0.04 e^- , respectively). As a result, C-N species have a positive effect towards facilitating the nucleation and uniform distribution of Li_2CO_3 by providing strong adsorption sites and enhancing the CRR kinetics.

In the CER, the adsorption energies show that C-N and C-F species exhibit strong interactions (−1.44 and −1.43 eV, respectively) with Li_2CO_3 , whereas graphene, C-O, and C-S species show weak interactions (Fig. 1b, blue bar). In addition, there is an evident charge transfer of 0.024 e^- from Li_2CO_3 to C-N species, which is significantly larger than that to graphene and C-F species (Fig. 1d), indicating that discharge products Li_2CO_3 on C-N species more easily lose electrons. It should be noted that the atomic configurations clearly show that there is a strong interaction between Li_2CO_3 and C-N species, revealing the weaker nature of the Li-O bonds and reduced decomposition energy barriers of Li_2CO_3 ^{24,25}. As a result, it is expected that C-N species can construct a bidirectional fast-electron migration bridge by providing strong adsorption sites and fast charge transfer capability to $^*\text{CO}_2^-$ and Li_2CO_3 , achieving boosted CRR/CER kinetics and enhanced interfacial catalytic properties.

Performance evaluation of single-salt electrolytes for Li-CO₂ cells

We proceeded to Li-CO₂ cells to verify the practicality of the above theoretical results. Various 1 M lithium salts (lithium nitrate (LiNO_3), or LiFSI, or lithium tetrafluoroborate (LiBF_4), or LiTFSI), in dimethyl sulfoxide (DMSO) solvent, were selected as electrolytes to manipulate the SEI composition on cathode surfaces. To better explore the key roles of the SEI components and detect them, commercial rGO with poor catalytic performance was employed as a matrix.

Figure 2 shows the overall electrochemical performance of the Li-CO₂ cells, with the cells using LiFSI electrolytes (denoted as LiFSI cell) delivering superior cycling and rate capabilities among the various electrolytes. Cycling performance was evaluated by limiting the cut-off specific capacity to 500 mA h g^{-1} . The long-term profiles show that the LiFSI cell notably delivers the longest lifetime of 90 cycles (900 h) at 0.1 A g^{-1} , which was twice that in the cell using LiNO_3 electrolytes, denoted as LiNO_3 cell, delivering 45 cycles (450 h) (Fig. 2a top and Supplementary Fig. 3). When the current density was increased to 0.2 A g^{-1} , the LiFSI cell could still run for 91 cycles compared to the other cells, in which the cycling performance was degraded (Fig. 2a bottom and Supplementary Fig. 4). This clearly demonstrates the substantial effects of different salts on battery cycling. The superior cycling performance of LiFSI cells is attributed to relatively high ionic conductivity of LiFSI electrolytes (10.93 mS cm^{-1} , Supplementary Fig. 5) and excellent reversibility of Li_2CO_3 during cycling in LiFSI cells, as supported by electrochemical impedance spectroscopy (EIS)^{8,23}. Full recovery of the impedance spectrum could only be observed for the

LiFSI cell (Fig. 2b) after a discharge-charge cycle compared with a partial recovery for the others (Supplementary Fig. 6), suggesting the complete decomposition of deposited Li_2CO_3 upon recharging in LiFSI cells. Furthermore, Supplementary Fig. 7 shows that the increase in impedance with cycling follows the trend of LiFSI < LiTFSI < LiBF_4 < LiNO_3 , consistent with their cycling profiles (cycle life decreases in the order of LiFSI > LiTFSI > LiBF_4 > LiNO_3). As expected, the impedances of LiFSI cells were maintained to be the lowest (Supplementary Fig. 7d), while those of LiNO_3 cells vastly increased just after 20 cycles (Supplementary Fig. 7a).

The excellent electrochemical performance of LiFSI cells was also revealed through full-discharge capability and rate performance. Figure 2c presents the full-discharge curves at 0.1 A g^{-1} , demonstrating that the LiFSI cell delivers the highest discharge capacity of 8,629.26 mA h g^{-1} compared to the others. Rate performance was evaluated at different current densities, from 0.1 to 2 A g^{-1} . At low current densities, the charge/discharge curves of the Li-CO₂ cells show similar overpotential. At a high current density of 2 A g^{-1} , however, a flat discharge voltage plateau (Fig. 2d) with a small overpotential (Fig. 2e) could only be found in the LiFSI cell. The cells with other electrolytes suffered from a dramatic decay of their discharge capacity at 2 A g^{-1} (Supplementary Figs. 8 and 9). To further test the effect of various electrolytes on battery performance, Li-CO₂ cells were also assembled by using carbon papers as matrix without catalysts (Supplementary Fig. 10) or using cathodes with Ru catalysts (Supplementary Fig. 11), respectively, which exhibited the same tendency of cycling performance as that using rGO as matrix. By using Ru as catalysts, the cells in LiFSI-based electrolytes maintain the cut-off capacity after 630 h at 0.3 A g^{-1} , whereas the cells in LiNO_3 -based electrolytes exhibit capacity decay after 250 h (Supplementary Fig. 11). The superior cycling stability of Li-CO₂ batteries with the LiFSI electrolyte may result from high reversibility of Li_2CO_3 in LiFSI cells, which enables a relatively low charge voltage for CER and thus suppresses electrolyte decomposition.

Cathode characterization to understand the correlation between reversibility of Li_2CO_3 and SEI composition

In-situ differential electrochemical mass spectrometry (DEMS) was first conducted to examine the reversibility of Li_2CO_3 in real time by monitoring CO_2 consumption, evolution, and the corresponding charge-to-mass ratios (e^-/CO_2). The collected gases in the in-situ DEMS results show that CO_2 was consumed in first battery discharge, and CO_2 was released in first battery recharge (Fig. 3a, b). The theoretical value of e^-/CO_2 ratio is 1.33 ($4e^-/3\text{CO}_2$), corresponding to the decomposition of Li_2CO_3 in accordance with the redox reaction of $3\text{CO}_2 + 4\text{Li}^+ + 4e^- \leftrightarrow 2\text{Li}_2\text{CO}_3 + \text{C}$ ²⁶. The deviation from the standard value of 1.33 indicates the occurrence of parasitic reactions. As shown in Fig. 3a, the e^-/CO_2 ratios in LiNO_3 cells deviated considerably from 1.33, which were determined as 1.09 and 1.72 for discharge and charge processes, respectively. In contrast, the ratios in the LiFSI cells were determined to be 1.327 and 1.5 during discharge and charge, respectively (Fig. 3b). The lower deviation from the standard e^-/CO_2 value in the LiFSI cell implies better reversibility of Li_2CO_3 and less electrolyte decomposition than that in the LiNO_3 cell, consistent with superior cycling performance of the LiFSI cell.

Furthermore, Li-CO₂ cells were disassembled after cycling for ex-situ cathode characterization to confirm the correlation between the reversibility of Li_2CO_3 and battery cycling performance. Scanning electron microscope (SEM) was performed on cathodes before (Supplementary Fig. 12) and after discharge (Supplementary Fig. 13), revealing discharge products deposited on cathode surfaces. Further detailed examination using high resolution transmission electron microscopy (TEM) confirmed this (Supplementary Fig. 14), with fast Fourier transform patterns in TEM images, containing rings correspond to the (101) and ($\bar{3}$ 12) lattice planes of Li_2CO_3 , which could verify

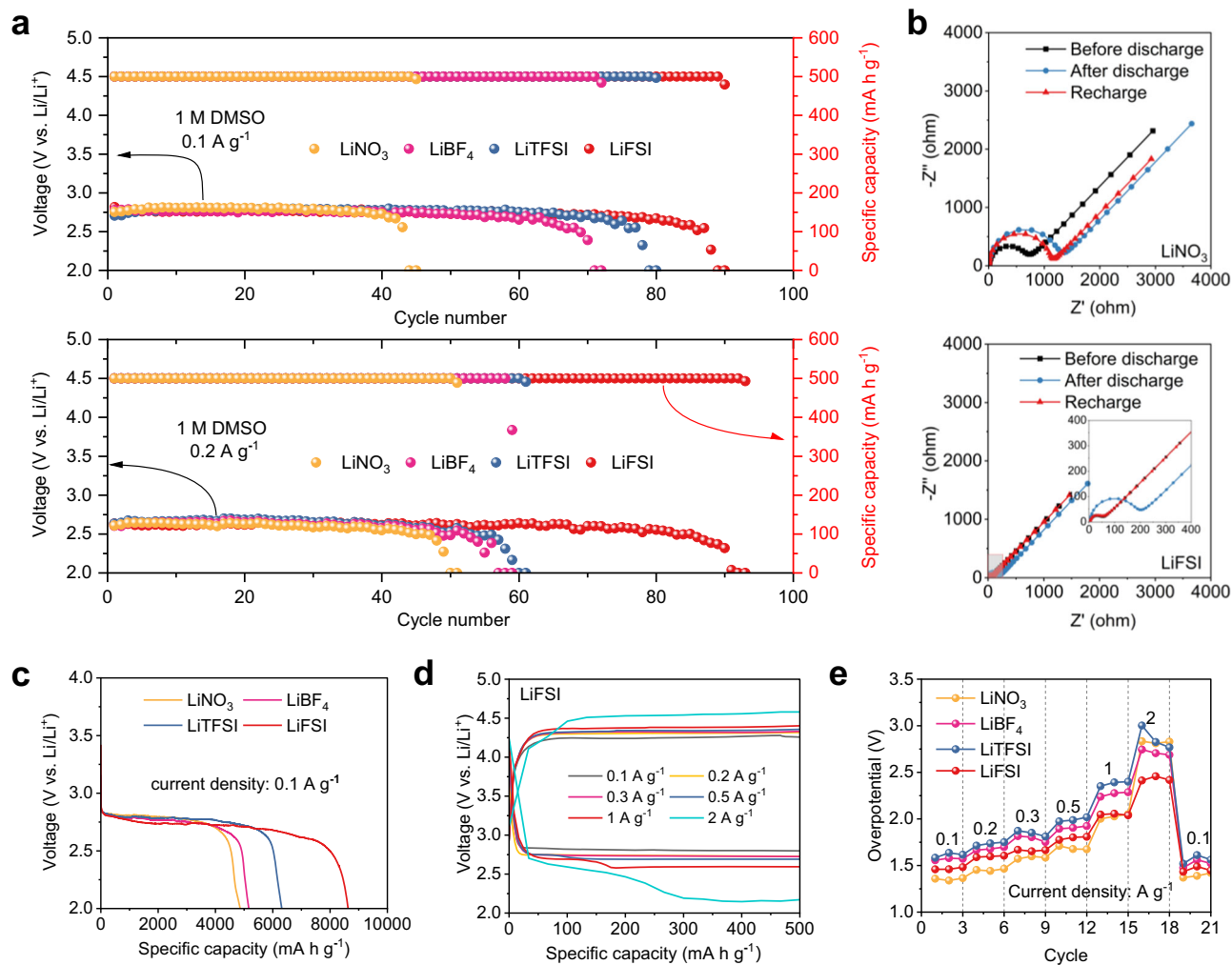


Fig. 2 | Electrochemical performance of Li-CO₂ cells in various electrolytes.

a Long-term cycling performance at 0.1 A g⁻¹ (top) and 0.2 A g⁻¹ (bottom) with a cut-off capacity of 500 mAh g⁻¹ (in the cut-off voltage from 2 V to 5 V). **b** EIS spectra of the LiNO₃ (top) and LiFSI (bottom) cells (the inset shows enlarged EIS spectra for LiFSI cells) before discharge, after the first discharge, and after recharge. **c** Full-

discharge curves at 0.1 A g⁻¹ with low cut-off voltage of 2 V. **d** Discharge-charge curves of the LiFSI cell taken at variant current densities (0.1–2 A g⁻¹ in the cut-off voltage from 2 V to 5 V). **e** Overpotential comparison of the various electrolytes at different current densities.

the formation of Li₂CO₃ as discharge product. The formation of Li₂CO₃ was also confirmed by the selected area electron diffraction (SAED) pattern (Supplementary Fig. 15), the newly emerged peaks at 860 cm⁻¹, 1412 cm⁻¹ and 1473 cm⁻¹ in the Fourier transform infrared (FTIR) spectra (Supplementary Fig. 16)²⁷, a peak located at 1089 cm⁻¹ in the Raman spectra (Supplementary Fig. 17)²⁸, and a peak at 290.6 eV in the X-ray photoelectron spectroscopy (XPS) spectra (Supplementary Fig. 18)^{29,30}. In order to eliminate the possible sample pollution, in-situ Raman evidence was provided for the Li-CO₂ cells to prove the formation/decomposition of Li₂CO₃ during battery cycling (Supplementary Fig. 19). Taking LiNO₃ and LiFSI electrolytes as examples, the peak of Li₂CO₃ can be clearly observed to emerge during discharge and gradually disappear during charging (Supplementary Fig. 20), suggesting the excellent reversibility of the cathodes. Furthermore, signals of DMSO₂ species (*) were detected, which suggests decomposition of DMSO solvent due to the attack of reduced *CO₂²⁻ radicals during cycling. Compared to the strong signals of DMSO₂ species in LiNO₃ cells, the signals in LiFSI cells gradually disappeared after being fully recharged, verifying that solvent degradation could be suppressed to some extent, in accord with its superior cycling stability.

After recharge, the cathodes nearly return to the pristine morphology (Supplementary Fig. 21). More importantly, the complete

Li₂CO₃ decomposition could only be observed in LiFSI cells, based on the disappearance of the Li₂CO₃ peak after cycling in FTIR (Supplementary Fig. 16) and Raman spectra (Supplementary Fig. 22), which indicates outstanding electrochemical reversibility of Li₂CO₃. In contrast, certain amounts of Li₂CO₃ residuals were still detected on the cycled cathodes in the other electrolytes. Examination of the C 1s XPS spectra further revealed the relationship between Li₂CO₃ residuals and battery cycling performance, in which the cells show the presence of Li₂CO₃ residuals except for the cell in LiFSI electrolytes (Fig. 3c left). Notably, the cells present cyclability decay as the intensity of Li₂CO₃ residuals peak becomes stronger, especially for the LiNO₃ cell, which displays the largest amount of Li₂CO₃ residuals and unsatisfactory cycling performance. These results cross-validated the importance of reversibility of Li₂CO₃ in determining cell capacity degradation and displayed consistency with their cycling profiles.

Based on our calculated results (Fig. 1), C-N species in SEIs can enhance interfacial catalytic properties to accelerate the CO₂ reaction kinetics, suggesting a positive correlation between C-N species and reversibility of Li₂CO₃. Therefore, SEI with a high content of C-N species ensures the complete decomposition of Li₂CO₃, thus resulting in excellent cycling capability. Ex-situ XPS analysis of cathodes before (Supplementary Fig. 23) and after cycling (Supplementary Fig. 24)

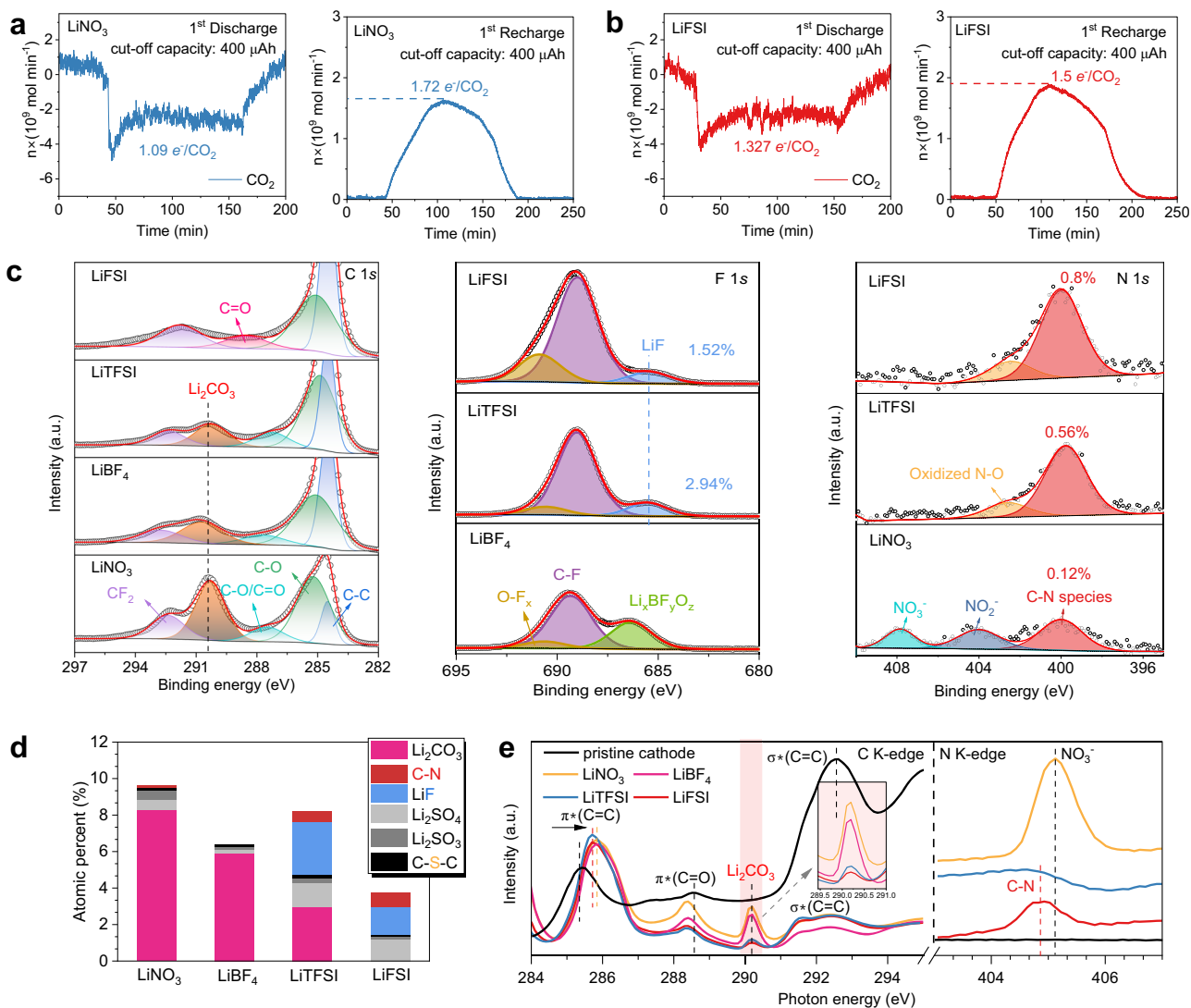


Fig. 3 | Characterization of discharge products and SEI composition on the cathodes. In-situ DEMS analyses of Li-CO₂ cells during first discharge/charge in **a** LiNO₃ and **b** LiFSI electrolytes, tested at 200 μ A within a capacity of 400 μ Ah. **c** C 1 s, F 1 s, and N 1 s XPS spectra for the cathodes after 3 cycles (Li₂CO₃: 290.6 eV, LiF: 685.5 eV, NO₂⁻: 403.8 eV, and NO₃⁻: 408.1 eV, respectively; the bonding

configuration of pyrrolic-N at -400.1 eV is in accord with C-N species)⁵⁴. **d** The compounds assigned to the C, N, F, and S elements and their relative amounts. **e** C K-edge and N K-edge XANES spectra for the pristine cathode and cathodes after 3 cycles. The peak of Li₂CO₃ was highlighted by red shade with enlargement in the range of 289.5–291 cm⁻¹ in the inset.

confirmed the composition of SEI, mainly consisting of LiF and C-N species (Fig. 3d). Indeed, it is generally known that LiF as a critical SEI component is beneficial to electrode stability and battery cycling^{15–19}. With lower LiF content (1.52%) on the cycled cathodes, however, it was surprisingly found that the cells in LiFSI electrolytes show better cycling stability than that in LiTFSI electrolytes with a higher LiF content (2.94%) on the cycled cathodes (Fig. 3c middle and Supplementary Fig. 25)³¹. This might offer a clue that the relative contents of C-N species in SEIs would affect the electrochemical performance to some extent, which is in good agreement with the calculated results related to the C-N species. As shown in Fig. 3c (right), the highest content of C-N species (0.8%) was detected on cathodes cycled in LiFSI cells, which delivers the longest cycle life. In comparison, a lower ratio of C-N species was found, 0.56% and 0.12% on cathodes cycled in LiTFSI and LiNO₃ cells, respectively, with both cells exhibiting relatively poor cycling performance^{32–34}. Energy dispersive spectroscopy (EDS) results also demonstrate the same trend relating to the N content on the surfaces of cathodes (Supplementary Figs. 26–29) with the most prominent N signal in the LiFSI cell. These results indicate the catalytic

effects of C-N species towards promoting the decomposition of Li₂CO₃ (Fig. 3c) and thus prolonging cycle life (Fig. 2a). In addition, the relatively lower peaks of C-S-C suggest that the decomposition of electrolyte is effectively suppressed in LiFSI electrolytes (Supplementary Fig. 30)¹⁶, consistent with the in-situ DEMS result (Fig. 3b).

To more deeply understand the effects of C-N species in SEIs on the cycling stability of Li-CO₂ batteries, X-ray absorption near-edge spectroscopy (XANES) was employed to trace the residuals of Li₂CO₃ and C-N species on cathodes after 3 cycles due to its high sensitivity for carbon detection³⁵. As shown in Fig. 3e, the C K-edge XANES spectra for the LiNO₃ and LiBF₄ cells displayed the strong peak of Li₂CO₃ at 290.2 eV on cathodes after cycling³⁶. In addition, the graphite π^* (C=C) transition on all cycled cathodes was observed with a slight shift to a higher photon energy compared to the pristine one, indicating an interaction between Li₂CO₃ residuals and rGO catalysts at surfaces. With the existence of C-N species, the cathode cycled in LiFSI-based electrolytes (red line) shows less shift of π^* (C=C) peak and much reduced intensity of π^* (C=O) peak than that in LiNO₃ cells (yellow line, without C-N species), indicating the weaker interaction between

Li_2CO_3 residuals and rGO catalysts, and possible strong interaction between Li_2CO_3 and C-N species³⁷, in good agreement with our calculation results. It should be noted that the intensities of Li_2CO_3 residuals gradually decreased with increased peak intensity of C-N species at 404.8 eV in the N K-edge XANES spectra³⁸, further confirming the catalytic effects of C-N species towards Li_2CO_3 decomposition. In particular, the cells in LiNO_3 and LiBF_4 electrolytes with low contents of C-N species show significantly high intensities of Li_2CO_3 residuals peaks (Fig. 3e, yellow and purple lines, respectively), suggesting their inferior reversibility of Li_2CO_3 and poor cycling stability. In contrast, the cells in LiFSI electrolytes with a relatively higher content of C-N species show the lowest intensities of Li_2CO_3 residuals (Fig. 3e, red lines), thus superior cycling performance. The XANES results are in accordance with the positive correlation between C-N species and Li_2CO_3 residuals in the XPS analysis (Fig. 3c). These observations identified the positive correlation between the content of C-N species in SEIs and reversibility of Li_2CO_3 , revealing that C-N species may play a critical role in enhancing reversibility of Li_2CO_3 and battery cyclability, which is in good agreement with our calculated results.

Relationship between electrolyte solvation structures and chemical composition of the SEI

Theoretical studies and experimental observations of electrolyte structures were employed to understand the origin of C-N species in SEIs in various electrolytes. Raman measurements were first conducted to study their solvation structures, showing various solvation structures in these electrolytes (Supplementary Fig. 31)³⁹, and providing the detailed information about the coordination environments of different anions. It has been widely accepted that a shift of an anion peak to higher wavenumbers in electrolytes indicates that the anion binds with Li^+ ions, and more shift suggests stronger Li^+ -anion interaction⁴⁰. With increasing shift, the interaction can be classified into free anion, solvent-separated ion pairs (SSIP), and contact ion pairs (CIP)⁴¹. As shown in Fig. 4a, LiNO_3 and LiFSI electrolytes show more CIP (52.5% and 44.65 %, respectively) relative to the other electrolytes, while a smaller proportion of CIP is observed in the others: LiTFSI (13.7 %) and LiBF_4 (12.4 %) (Supplementary Tables 2 and 3). This demonstrates that NO_3^- and FSI^- have the strongest coordination with Li^+ ions compared to the others, which can promote anion-derived SEI generation on electrodes.

Molecular dynamics (MD) and radial density function (RDF) investigations further reveal the structure of solvation shells and overall electrolyte configurations. In RDFs (Supplementary Fig. 32), the sharp peaks at around 2 Å for Li-anion coordination indicate the existence of all the anions in the inner solvation shell, and their intensities decrease in the order of $\text{LiNO}_3 > \text{LiBF}_4 > \text{LiFSI} > \text{LiTFSI}$. The corresponding coordination numbers of anions confirm the trend, as shown in Fig. 4b (yellow columns). Taking LiNO_3 and LiFSI electrolytes as examples, the average coordination number is 2.31 for LiNO_3 versus 1.42 for LiFSI, indicating large amounts of anions in inner solvation shells. Furthermore, more information was provided by the surrounding environment of Li^+ solvation clusters, which can be classified as solvent-surrounded Li^+ , Li^+ -single anion pair, and Li^+ -multiple anion cluster by coordination numbers of anions with Li^+ ions of 0, 1, and ≥ 2 (Supplementary Table 4). The most probable Li^+ solvation clusters are Li^+ -single anion pairs and Li^+ -multiple anion clusters for LiNO_3 , LiBF_4 , and LiFSI electrolytes (Fig. 4c–e), whereas solvent-surrounded Li^+ clusters dominate for the LiTFSI electrolyte (Fig. 4f). In particular, a large preference for Li^+ solvation clusters including anions (50% Li^+ -single anion pairs and 36% Li^+ -multiple anion clusters) is for LiFSI (Fig. 4f), which agrees with the high content of CIP (44.65 %) in the Raman results (Fig. 4a) and distinct ^{19}F NMR peaks from FSI^- corresponding to the Li- FSI^- coordination (Supplementary Fig. 33). Overall, both theoretical calculation and experiment results demonstrate that the solvation shells in LiNO_3 and LiFSI electrolytes contain more anions

around Li^+ ions, which is promising for a preferentially anion-derived SEI on electrodes.

To explain why the content of C-N species in LiFSI is higher than that in LiNO_3 electrolytes (as demonstrated in Fig. 3c, right), density functional theory (DFT) calculations were performed to investigate the bonding strength between Li^+ ion and different anions. The binding free energy (ΔG_{bind}) was calculated between one Li^+ ion and one anion to examine the bonding strength of different anions with an Li ion (Supplementary Fig. 34)⁴⁰. All Li^+ -anion complexes show negative ΔG_{bind} (Supplementary Fig. 35), and a more negative ΔG_{bind} suggests a stronger coordination of anions with Li^+ ion in the solvation shell. Compared to all the other anions, NO_3^- shows the most negative ΔG_{bind} of -0.83 eV, whereas FSI shows the least negative ΔG_{bind} of -0.43 eV (Fig. 4b, green columns). The relatively high ΔG_{bind} suggests that FSI preferentially desolvates with Li^+ ion than other anions, and then decomposes on the cathode surface, leading to a high content of C-N species in SEI layer^{13,42}. This reveals that the decomposition reactions not only depend on the solvation structure, but also the coordination capability between different components in inner solvation shells.

Based on the discussion in the characterization part, we believe that in-situ formed C-N species in SEIs could enhance the reversibility of Li_2CO_3 , thus improving the cycling performance of Li- CO_2 batteries. To achieve high content of C-N species in SEIs, electrolyte design for Li- CO_2 batteries may obey the following principles: First, the employment of electrolyte salt with nitrogen-containing anions is the key to forming C-N species in SEI layers. Second, involvement of N-containing anions in Li^+ solvation shells, reflected by coordination numbers and surrounding environment of Li^+ solvation clusters, ensures the formation of anion-derived SEI layers containing C-N species. Finally, a high binding free energy between Li ion and anion, gives an estimate of coordination capability and weak Li-anion interaction in inner solvation shells, suggesting preferentially anion-derived SEI formation.

Synergistic effect of C-N species and LiF components of SEI in dual-salt electrolytes

Given the electrolyte design principles discussed above, we developed 1 M dual-salt (including LiNO_3 and LiTFSI, LiBF_4 and LiTFSI, LiNO_3 and LiFSI, LiBF_4 and LiFSI, as shown in Supplementary Fig. 36) electrolytes in expectation of further improvements in battery performance through increasing the involvement of N-containing anions in solvation shells to generate a C-N rich SEI on cathodes. We found that the cells using $\text{LiNO}_3/\text{LiFSI}$ dual-salt electrolytes perform a distinct improvement in electrochemical performance. Notably, the cell in 0.25 M $\text{LiNO}_3/0.75$ M LiFSI electrolytes exhibits the highest amount of C-N species (Fig. 5c, d) and delivers the best cycling performance, which is in good agreement with our rationale.

With the addition of LiNO_3 , there is substantial improvement in battery performance (Supplementary Fig. 37). The Li- CO_2 cell in an optimized dual-salt electrolyte with 0.25 M $\text{LiNO}_3/0.75$ M LiFSI can be charged/discharged up to 150 cycles (1500 h) (Fig. 5a), significantly improving the cycle life compared to that using the best single-salt electrolyte (LiFSI, 900 h). Supplementary Fig. 38 displays the obvious superiority of dual-salt electrolytes in terms of full-discharge capacity, especially the highest capacity of 15,127.9 mA h g^{-1} , which was realized in the 0.25 M $\text{LiNO}_3/0.75$ M LiFSI cell. The superior performance of dual-salt electrolytes was also demonstrated by their rate capability (Supplementary Fig. 39), in which the 0.25 M $\text{LiNO}_3/0.75$ M LiFSI cell exhibits a much lower overpotential than the single-salt LiFSI cell among all the current densities (Supplementary Fig. 40). Moreover, electrode with Ru nanoparticles without further modification as catalysts was applied to lower the overpotential and enhance the cyclability of Li- CO_2 batteries, it performed 2200 h of cycling with 1 V overpotential in the first 40 cycles (Supplementary Fig. 41). Overall, batteries with the 0.25 M $\text{LiNO}_3/0.75$ M LiFSI electrolyte show improved battery lifespan, reduced overpotential, and lower

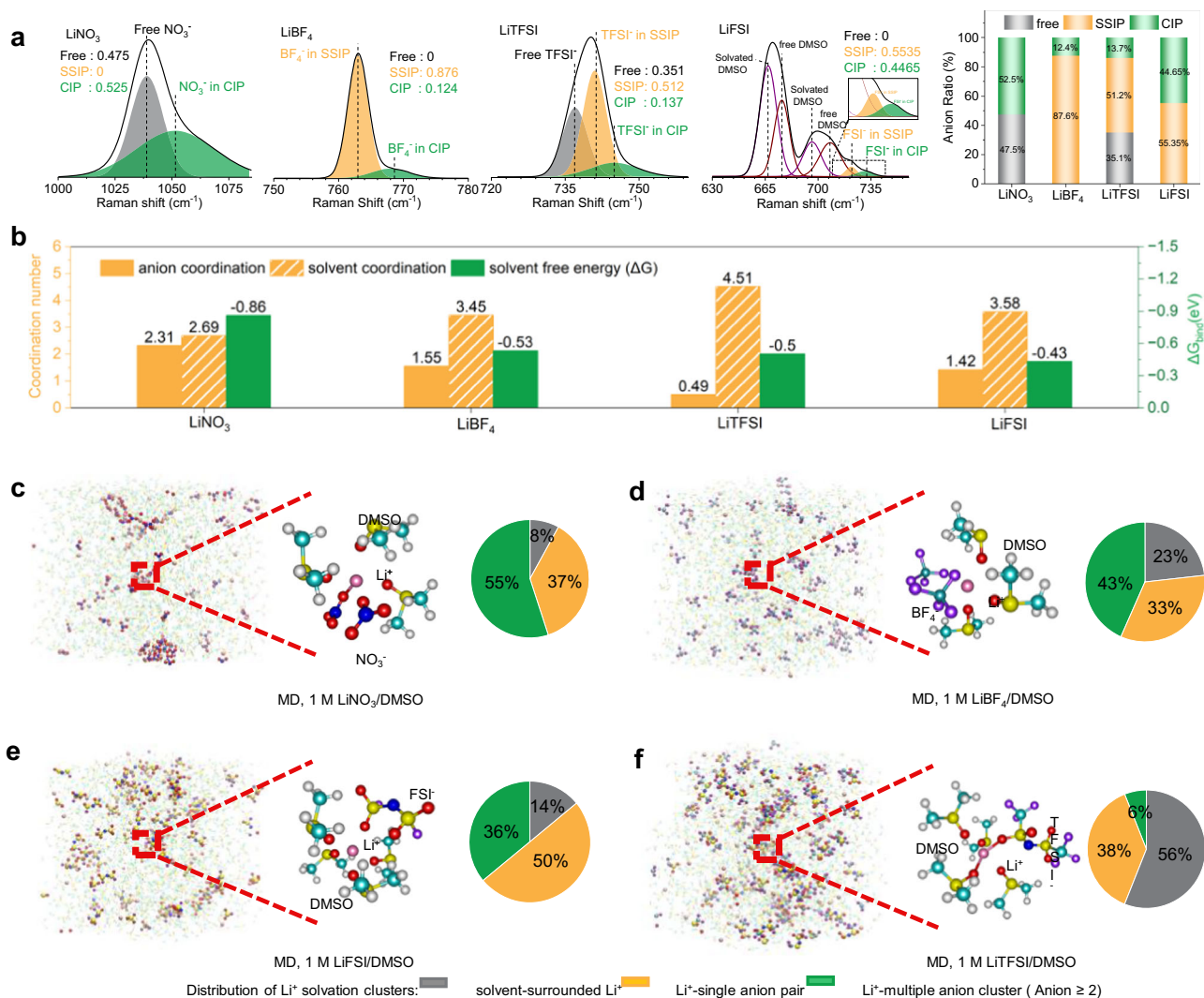


Fig. 4 | Theoretical and experimental studies on the Li^+ solvation structures and electrolyte configurations. **a** Fitted Raman curves of anions for different anion pairs of free anions, SSIP (solvent-separated ion pairs), and CIP (contact ion pairs), and their ratio comparison, with enlargement in the range of 710–745 cm^{-1} for the LiFSI electrolyte in the inset. The peaks located at 667 and 697 cm^{-1} can be assigned to the C-S symmetric and asymmetric stretching vibrations of free DMSO, respectively. The peaks at 676 and 708 cm^{-1} are attributed to the C-S symmetric and asymmetric stretching vibrations of DMSO molecules that solvate with Li^+

ions^{17,39,55,56}. **b** Left Y-axis: coordination numbers of different anions (yellow) and DMSO solvent (yellow slashes) in inner solvation shells by MD; right Y-axis: Binding free energy ΔG_{bind} between Li^+ and different anions calculated by DFT. MD simulation boxes, representative structures of Li^+ solvation clusters, and the electrolyte configurations based on the percentages of different Li^+ solvation clusters for **c** LiNO_3 , **d** LiBF_4 , **e** LiFSI , and **f** LiTFSI electrolytes. Colour scheme of molecules: Li, pink; C, light blue; H, white; O, red; N, navy; S, yellow; F, purple; and B, blue.

estimated cost due to relative low price of LiNO_3 (Supplementary Table 5), suggesting its suitability as electrolyte for Li-CO_2 batteries (Fig. 5b).

To verify the positive effect of C-N species towards enhanced battery performance in dual-salt electrolytes, the correlation between the reversibility of Li_2CO_3 and the content of C-N species in SEIs was first analysed. After 3 cycles, the XANES spectra show that the intensities of Li_2CO_3 residuals in the C K-edge spectra decreased with increased peak intensity of C-N species in the N K-edge spectra (Fig. 5c). More importantly, no Li_2CO_3 residuals in the C K-edge XANES spectrum could be detected in the 0.25 M $\text{LiNO}_3/0.75 \text{ M LiFSI}$ cell, which displays the most distinguish peak of C-N species and superior cycling performance. The positive effect of C-N species towards battery cycling can be also confirmed by XPS spectra, displaying no Li_2CO_3 residuals in cells using dual-salt electrolytes, even after 50 cycles (Supplementary Figs. 42 and 43). Compared to the XPS results of single-salt LiFSI electrolytes (0.8% C-N species), the XPS results of

dual-salt electrolytes after 3 cycles present a relatively higher content of C-N species (1.1% for the 0.25 M $\text{LiNO}_3/0.75 \text{ M LiFSI}$ cell and 0.89% for the 0.75 M $\text{LiNO}_3/0.25 \text{ M LiFSI}$ cell) (Supplementary Fig. 44), consistent with their relatively long cycle life. These results confirm the catalytic effect of C-N species towards promoting Li_2CO_3 decomposition and prolonging battery cycling. Interestingly, except for increased content of C-N species, we found that relatively higher amounts of LiF were observed on the cathodes cycled in the cells using dual-salt electrolytes (Supplementary Figs. 45 and 46) compared with that of the single-salt LiFSI cell (Fig. 3c, middle). This suggests less electrolyte consumption owing to the effective protection to electrodes from LiF -rich SEI layers, which can be evidenced by the lowest intensity of the by-products from solvent (DMSO) decomposition, such as C-S-C (Supplementary Fig. 47). In-situ DEMS results further proved better reversibility of Li_2CO_3 and less electrolyte decomposition in cells using dual-salt electrolytes. Taking the 0.25 M $\text{LiNO}_3/0.75 \text{ M LiFSI}$ electrolytes as an example, its e^-/CO_2 was determined to be 1.3 during

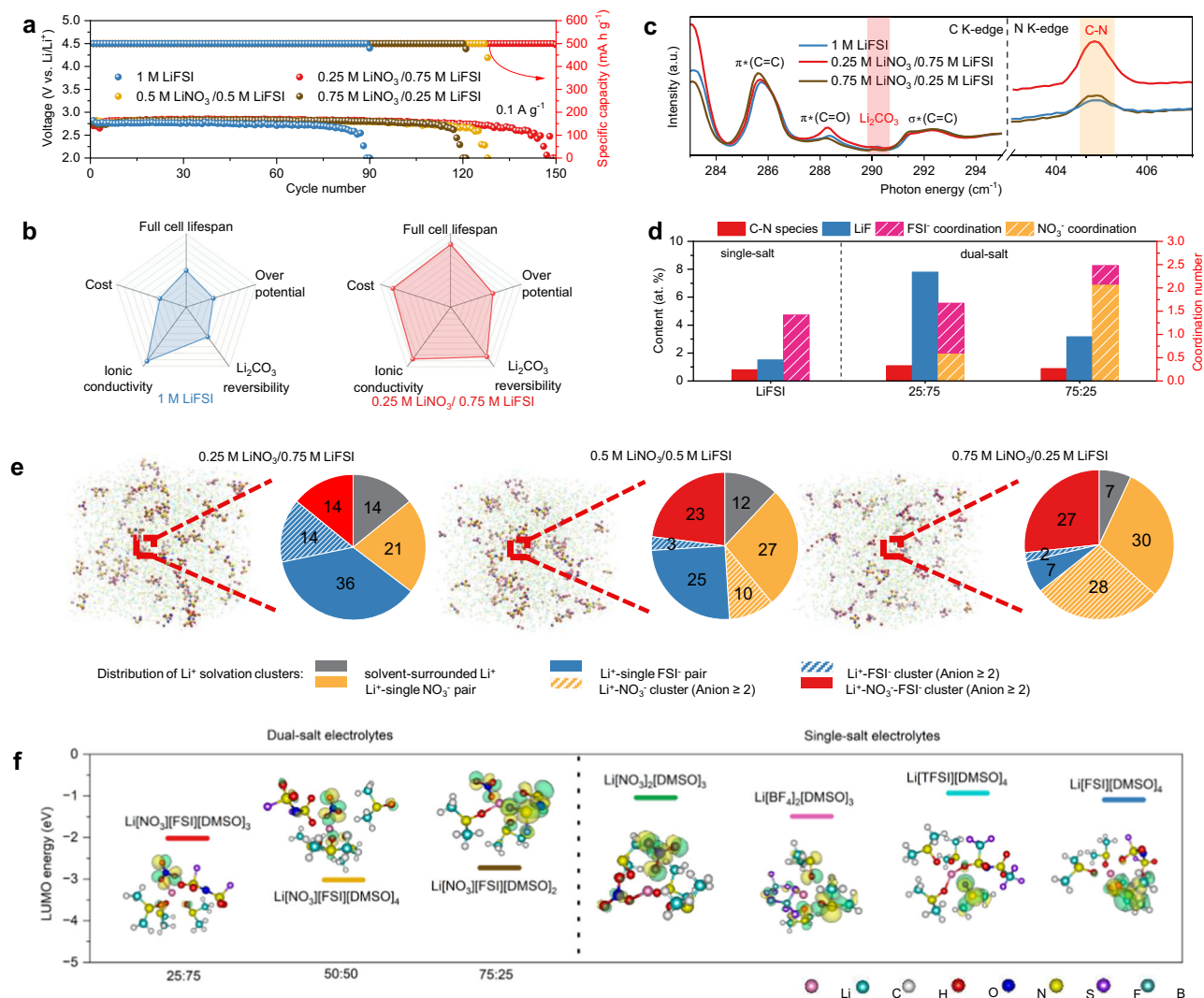


Fig. 5 | Summary and overall evaluation of dual-salt electrolytes. **a** Long-term cycling performance at 0.1 A g⁻¹ with a cut-off capacity of 500 mAh g⁻¹ (in the cut-off voltage from 2 V to 5 V). **b** Overall comparison of the properties and performances of the LiFSI electrolyte and 0.25 M LiNO₃/0.75 M LiFSI electrolyte. **c** C K-edge and N K-edge XANES spectra for the cathodes after 3 cycles in single-salt LiFSI and dual-salt electrolytes. **d** Comparison of C-N species and LiF content on cathodes after 3 cycles in single-salt LiFSI and dual-salt electrolytes, and their coordination numbers

of anions for these electrolytes. **e** MD simulation boxes and the corresponding percentages of different Li⁺ solvation clusters in dual-salt electrolytes. **f** LUMO energy values for representative Li⁺ solvation clusters in single-salt and dual-salt electrolytes. Colour scheme of molecules: Li, pink; C, light blue; H, white; O, red; N, navy; S, yellow; F, purple; and B, blue. The yellow and blue zones represent electron loss and gain, respectively.

recharging (Supplementary Fig. 48). It is very close to the theoretical value of 1.33 ($4e^-/3CO_2$) as the reversible decomposition of Li₂CO₃, indicating its excellent reversibility of Li₂CO₃ and high electrolyte stability. As summarized in Fig. 5d and Supplementary Fig. 49, C-N and LiF-rich SEI layers on cathodes were constructed in dual-salt electrolytes, which can not only achieve a highly reversible Li₂CO₃ formation/decomposition behaviour but also effectively suppress electrolyte consumption, thus achieving improved cycling performance of Li-CO₂ battery via the synergistic effect of C-N species and LiF components in SEI layer. To better offer direct evidence of the positive effect of C-N species towards battery cycling, we have conducted additional work comparing the cycling performance of Li-CO₂ cells using uncycled cathodes and cathodes, after the formation of C-N species in SEI layers (the cathodes after 5 cycles in the Li-CO₂ cells using the optimized 0.25 M LiNO₃/0.75 M LiFSI electrolytes, denoted as cathodes with C-N species). This was done using conventional electrolytes (1 M LiTFSI/DMSO and 1 M LiTFSI/TEGDME, which have been widely used in Li-CO₂ batteries). To eliminate the possible effects from the passivation of the

Li anode by electrolytes, all the cells were paired with fresh Li metal. When paired with cathodes with C-N species, substantial improvement in battery cycling occurred, even in conventional electrolytes, as summarized in Supplementary Table 6, Supplementary Figs. 50 and 51.

To understand the origin of increased contents of C-N species and LiF in dual-salt electrolytes, MD simulations and DFT calculations were jointly employed to unveil the SEI formation mechanisms. MD simulations predict the existence of (Li⁺-NO₃⁻-FSI⁻) clusters in dual-salt electrolytes (Fig. 5e), which present a reduced lowest unoccupied molecular orbital (LUMO) energy (from -2.02 to -3.03 eV) than (Li⁺-anions) in single-salt electrolytes (from -0.93 to -1.49 eV) (Fig. 5f and Supplementary Fig. 52). This indicates that the anions in these clusters exhibit an increased regional electrophilicity due to the participation of NO₃⁻ in solvation shells, leading to their higher possibility of accepting electrons⁴³. Therefore, the decomposition of FSI⁻ in (Li⁺-NO₃⁻-FSI⁻) solvation clusters can be greatly promoted, explaining the increased amounts of C-N species and LiF in dual-salt electrolytes (Fig. 5d). In addition, we found that coordination numbers of anions

(NO₃⁻ and FSI⁻) in dual-salt electrolytes are higher than that for the single-salt LiFSI electrolytes (Supplementary Fig. 53), suggesting their greatly increased nitrogen-containing anions in solvation shells. More importantly, compared to the other dual-salt electrolytes, 0.25 M LiNO₃/0.75 M LiFSI electrolytes show the largest coordination number of FSI⁻ anions (1.07) (Fig. 5d, purple slashes columns) and the highest proportion of the clusters including FSI⁻ (36% Li⁺-single FSI⁻ pairs + 14% Li⁺-multiple FSI⁻ clusters + 14% Li⁺-NO₃⁻-FSI⁻ clusters) (Fig. 5e, blue and red pies, and Supplementary Table 7). This suggests its highest amounts of C-N species and LiF in SEIs, consist with our experimental XPS results (Fig. 5d, red and blue columns). Benefited from the anion-derived dense SEI layers formed on cathodes, SEI layer on cathodes in dual-salt electrolyte, exhibits enhanced catalytic and protective properties, therefore, Li-CO₂ battery exhibits improved overall electrochemical stability compared to that in single-salt electrolytes.

Discussion

In summary, the critical roles of organic C-N species in facilitating the CO₂ reaction kinetics and achieving high reversibility of Li₂CO₃ has been demonstrated in this work. Through manipulating the SEI components on cathodes, the experimental results revealed the positive correlation between C-N species in the SEI and battery cycling, as demonstrated by the fact: an LiFSI-based cell with relatively high C-N species and low LiF in its SEI layer could deliver superior cycling performance to that of a LiTFSI-based cell with low C-N species and high LiF. Further theoretical calculations revealed the underlying mechanism: C-N species show strong adsorption towards CO₂ and *CO₂²⁻ to promote initial activation of the reaction and charge transfer in the CRR process, driving spontaneous and fast reduction reaction kinetics. In addition, the strong interaction between C-N species and Li₂CO₃ could build a bridge to enable fast charge transfer and high catalytic activity in the CER, which can further effectively enhance the Li₂CO₃ decomposition kinetics and thus the cycling performance. Dual-salt (LiNO₃/LiFSI) electrolytes were designed to further improve cyclability through increasing the contents of C-N species. The 0.25 M LiNO₃/0.75 M LiFSI cell exhibits stable cycling over 220 cycles (2200 h) with 1 V overpotential. Our findings provide a deep understanding of the correlation between the organic SEI components and battery performance, thus offering an electrolyte design principle to overcome the critical issues facing Li-CO₂ batteries for future applications.

Methods

Preparation of electrolytes

Dimethyl sulfoxide (DMSO) (Sigma-Aldrich, 99.9%) was dried twice over freshly activated 4 Å molecular sieves. Lithium nitrate (LiNO₃, ≥ 99.0%, ReagentPlus®, Sigma-Aldrich), lithium tetrafluoroborate (LiBF₄, 98%, Sigma-Aldrich), lithium bis(trifluoromethanesulfonyl) imide (LiTFSI, 99.95%, Sigma-Aldrich), and lithium bis(fluorosulfonyl) imide (LiFSI, 99.5%, Canrd) were dried under vacuum at 80 °C overnight. All electrolytes were prepared and stored in an Ar-filled glove-box (O₂ and H₂O levels < 0.01 ppm). All the electrolytes were composed of 1 M lithium salt(s) in DMSO solvent.

Preparation of cathodes

The air cathodes were prepared via a filtration process. Typically, 5 mg of catalyst materials (reduced graphene oxide, rGO) and 50 μL of Nafion solution (~5 wt%) were dispersed in 2 mL of ethanol. After being ultrasonicated for around 60 min, the suspension was filtered using Toray carbon paper (TGP-H-060) as the filtering paper. After being dried at 80 °C overnight, the catalyst was uniformly coated on the Toray carbon paper. The catalyst-loaded Toray carbon paper was then punched out into circular sheets with a diameter of 9 mm, which were directly used as air cathodes. Here, the Toray carbon paper served as the gas diffusion layer and current collector for the air cathodes.

Electrochemical measurements

For electrochemical tests, CR2032-type coin cells (16 holes on the cathode side) were assembled in an Ar-filled glove box with air electrodes and lithium chip anodes separated by a glass fibre separator (Whatman, diameter: 19 mm). Solutions of 1 M lithium salts in 1 L DMSO solvent were used as electrolytes. The as-prepared coin cells were sealed in CO₂-filled bottles for Li-CO₂ battery tests. The galvanostatic discharge/charge tests were carried out with high cut-off voltage of 5 V and low cut-off voltage of 2 V at various current densities (from 0.1 to 2 A g⁻¹) using a battery test station (Land, China) at 25 °C. Electrochemical impedance spectroscopy (EIS) was performed over the frequency range of 100 kHz to 10 MHz with a perturbation amplitude of ±10 mV using a VMP3 potentiostat/galvanostat (BioLogic).

Characterization

Raman spectra were collected on a Raman spectrometer (HORIBA LabRAM HR Evolution) using the 532 nm line of a semiconductor laser (100 MW, frequency-doubled Nd: YAG laser from Laser Quantum). The attenuated total reflection (ATR)-FTIR spectra were obtained using a Nicolet 6700 ThermoFisher instrument. The morphologies of the cathodes were investigated using field-emission scanning electron microscopy (FESEM, FEI QUANTA 450 FEG) and a cryo-transmission electron microscope (TEM). The cryo-TEM characterization was performed on a Thermo Scientific Glacios microscope with an accelerating voltage of 200 kV. High-resolution TEM images were obtained using a Thermo Scientific Falcon 4 camera at a dose rate of ~6 e⁻¹ px⁻¹ s⁻¹ with a dosage of ~40 eÅ⁻². X-ray photoelectron spectroscopy was conducted to analyse the chemical composition on the surface of the pristine and cycled cathodes on a VG Multilab 2000 (VG) photoelectron spectrometer using monochromatic Al Kα radiation under vacuum of 2 × 10⁻⁶ Pa. Ex-situ synchrotron X-ray absorption spectroscopy was carried out at the soft X-ray beamline, Australian Synchrotron. The conductivity of electrolytes was obtained from a conductivity measurement instrument (DDB-303A, Shanghai INESA & Scientific Instrument Co. LTD).

Theoretical calculations

All MD simulations were performed in the GROMACS package using the Optimized Potentials for Liquid Simulations (OPLS) force field. ACPYPE⁴⁴ was employed to obtain the force field topology along with the previously developed force field topology for BF₄⁻⁴⁵. A simulation box size of 5 × 5 × 5 nm³ was used in all simulation models. Further details on the ratios of electrolyte components and MD simulation parameters are available in the Supporting Information.

DFT calculations were implemented using the Vienna ab-initio simulation package (VASP 5.4.4)^{46,47} with the core and valence electronic interactions being modelled using the projector augmented wave (PAW) method^{48,49}. The Perdew-Burke-Ernzerhof (PBE) exchange-correlation function was employed⁵⁰. Molecular orbital energy levels (*i.e.*, LUMO) and different species interactions in solution were calculated using VASP with a kinetic energy cut-off of 500 eV and a single Gamma k-point. For the interaction between Li⁺ and other components in the electrolyte, including anion and solvent molecules, the thermodynamic cycle presented in Supplementary Figs. 34 and 35 was used, with the following Eq. 1:

$$\Delta G_{\text{bind}} = -G_{\text{DFT}} + G_{\text{Li vap}} + G_{\text{Li ion}} + G_{\text{Li solv}} \quad (1)$$

where G_{DFT} , $G_{\text{Li vap}}$, $G_{\text{Li ion}}$, $G_{\text{Li solv}}$ represent the electronic energy obtained from DFT calculations, Li vaporization energy from solid to gas, Li ionization energy from the atomic to the ionic state, and the approximation of Li ion solvation energy in the organic solvent^{51,52}.

For the interaction between different species and graphene as an electrode, a vacuum region of 20 Å was introduced in the direction of the z-axis to avoid interactions between periodic images.

The wavefunction was expanded with a kinetic energy cut-off of 500 eV, and a Gamma k-point mesh of $3 \times 3 \times 1$ was used. Geometrical optimizations were achieved by relaxing all ionic positions and supercell vectors until the Hellmann-Feynman forces were less than $0.01 \text{ eV } \text{\AA}^{-1}$. The dispersion correction was also considered in this study by using the DFT-D3 method⁵³. The adsorption energy was calculated by using the following Eq. 2:

$$E_{\text{ads}} = E(\text{graphene} * \text{adsorbate}) - E(\text{graphene}) - E(\text{adsorbate}) \quad (2)$$

where graphene represents all different functional graphene investigated here (Fig. S2) and adsorbates include Li, CO_2^{2-} , CO_3^{2-} , and Li_2CO_3 . The zero-point energy and entropic contributions at 298 K as well as the solvation correction for CO_2 were considered in the calculations of adsorption energy.

Reporting summary

Further information on research design is available in the Nature Portfolio Reporting Summary linked to this article.

Data availability

Source data are provided with this paper. All other data are available from the authors upon reasonable request. Source data are provided with this paper.

References

- Rogelj, J. et al. A new scenario logic for the Paris Agreement long-term temperature goal. *Nature* **573**, 357–363 (2019).
- Matthews, H. D. & Wynes, S. Current global efforts are insufficient to limit warming to 1.5 C. *Science* **376**, 1404–1409 (2022).
- Wang, Y. et al. The size of the land carbon sink in China. *Nature* **603**, E7–E12 (2022).
- Zhu, Q. et al. Enhanced CO_2 utilization in dry reforming of methane achieved through nickel-mediated hydrogen spillover in zeolite crystals. *Nat. Catal.* **5**, 1030–1037 (2022).
- Wang, S. et al. Highly selective hydrogenation of CO_2 to propane over $\text{GaZrO}_x/\text{H-SSZ-13}$ composite. *Nat. Catal.* **5**, 1038–1050 (2022).
- Zhang, W. et al. High-Performance K- CO_2 Batteries Based on Metal-Free Carbon Electrocatalysts. *Angew. Chem. Int. Ed.* **59**, 3470–3474 (2020).
- Wang, D. et al. A low-charge-overpotential lithium- CO_2 cell based on a binary molten salt electrolyte. *Energy Environ. Sci.* **14**, 4107–4114 (2021).
- Qie, L. et al. Highly Rechargeable Lithium- CO_2 Batteries with a Boron- and Nitrogen-Codoped Holey-Graphene Cathode. *Angew. Chem. Int. Ed.* **56**, 6970–6974 (2017).
- Zhou, J. et al. A Quasi-Solid-State Flexible Fiber-Shaped Li- CO_2 Battery with Low Overpotential and High Energy Efficiency. *Adv. Mater.* **31**, 1804439 (2019).
- Khurram, A., He, M. & Gallant, B. M. Tailoring the Discharge Reaction in Li- CO_2 Batteries through Incorporation of CO_2 Capture Chemistry. *Joule* **2**, 2649–2666 (2018).
- Zou, J. et al. Revisiting the Role of Discharge Products in Li- CO_2 Batteries. *Adv. Mater.* **35**, 2210671 (2023).
- Zhang, F. et al. Recent Progress and Future Advances on Aqueous Monovalent-Ion Batteries towards Safe and High-Power Energy Storage. *Adv. Mater.* **34**, 2107965 (2022).
- Yu, Z. et al. Rational solvent molecule tuning for high-performance lithium metal battery electrolytes. *Nat. Energy* **7**, 94–106 (2022).
- Zhang, W., Lu, J. & Guo, Z. Challenges and future perspectives on sodium and potassium ion batteries for grid-scale energy storage. *Mater. Today* **50**, 400–417 (2021).
- Yang, Y. et al. Armor-like Inorganic-rich Cathode Electrolyte Interphase Enabled by the Pentafluorophenylboronic Acid Additive for High-voltage Li||NCM622 Batteries. *Angew. Chem. Int. Ed.* **62**, 202300057 (2023).
- Chen, J. et al. Electrolyte design for LiF-rich solid–electrolyte interfaces to enable high-performance micro-sized alloy anodes for batteries. *Nat. Energy* **5**, 386–397 (2020).
- Zhang, W. et al. Regulating the reduction reaction pathways via manipulating the solvation shell and donor number of the solvent in Li- CO_2 chemistry. *Proc. Nat. Acad. Sci.* **120**, 2219692120 (2023).
- Liu, Y. et al. Self-assembled monolayers direct a LiF-rich interphase toward long-life lithium metal batteries. *Science* **375**, 739–745 (2022).
- Liang, J. Y. et al. Enabling a durable electrochemical interface via an artificial amorphous cathode electrolyte interphase for hybrid solid/liquid lithium-metal batteries. *Angew. Chem. Int. Ed.* **132**, 6647–6651 (2020).
- Shan, X. et al. A Brief Review on Solid Electrolyte Interphase Composition Characterization Technology for Lithium Metal Batteries: Challenges and Perspectives. *J. Phys. Chem. C.* **125**, 19060–19080 (2021).
- Hou, Y. et al. $\text{Mo}_2\text{C}/\text{CNT}$: An Efficient Catalyst for Rechargeable Li- CO_2 Batteries. *Adv. Funct. Mater.* **27**, 1700564 (2017).
- Mu, X. et al. Li- CO_2 and Na- CO_2 Batteries: Toward Greener and Sustainable Electrical Energy Storage. *Adv. Mater.* **32**, 1903790 (2020).
- Jin, Y. et al. High-Performance Li- CO_2 Batteries Based on Metal-Free Carbon Quantum Dot/Holey Graphene Composite Catalysts. *Adv. Funct. Mater.* **28**, 1804630 (2018).
- Zhou, G. et al. Theoretical calculation guided design of single-atom catalysts toward fast kinetic and long-life Li-S batteries. *Nano Lett.* **20**, 1252–1261 (2019).
- Xu, A. et al. Copper/alkaline earth metal oxide interfaces for electrochemical CO_2 -to-alcohol conversion by selective hydrogenation. *Nat. Catal.* **5**, 1081–1088 (2022).
- Li, X. et al. Artificial solid-electrolyte interphase and bamboo-like N-doped carbon nanotube enabled highly rechargeable K- CO_2 batteries. *Adv. Funct. Mater.* **32**, 2105029 (2022).
- Qiao, Y. et al. Li- CO_2 Electrochemistry: A New Strategy for CO_2 Fixation and Energy Storage. *Joule* **1**, 359–370 (2017).
- Ye, F. et al. Topological Defect-Rich Carbon as a Metal-Free Cathode Catalyst for High-Performance Li- CO_2 Batteries. *Adv. Energy Mater.* **11**, 2170120 (2021).
- Qiao, Y. et al. 3D-Printed Graphene Oxide Framework with Thermal Shock Synthesized Nanoparticles for Li- CO_2 Batteries. *Adv. Funct. Mater.* **28**, 1805899 (2018).
- Zhang, J. et al. Rechargeable Li- CO_2 Batteries with Graphdiyne as Efficient Metal-Free Cathode Catalysts. *Adv. Funct. Mater.* **31**, 2101423 (2021).
- Dong, T. et al. A multifunctional polymer electrolyte enables ultra-long cycle-life in a high-voltage lithium metal battery. *Energy Environ. Sci.* **11**, 1197–1203 (2018).
- Li, Y. et al. Highly Surface-Wrinkled and N-Doped CNTs Anchored on Metal Wire: A Novel Fiber-Shaped Cathode toward High-Performance Flexible Li- CO_2 Batteries. *Adv. Funct. Mater.* **29**, 1808117 (2019).
- Qiao, Y. et al. Synergistic effect of bifunctional catalytic sites and defect engineering for high-performance Li- CO_2 batteries. *Energy Storage Mater.* **27**, 133–139 (2020).
- Guo, Z. et al. A Highly Reversible Long-Life Li- CO_2 Battery with a RuP_2 -Based Catalytic Cathode. *Small* **15**, 1803246 (2019).
- Iputera, K. et al. Revealing the absence of carbon in aprotic Li- CO_2 batteries: A mechanism study toward CO_2 reduction under a pure CO_2 environment. *J. Mater. Chem. A* **10**, 3460–3468 (2022).
- Zhang, X. et al. Breaking the Stable Triangle of Carbonate via W–O Bonds for Li- CO_2 Batteries with Low Polarization. *ACS Energy Lett.* **6**, 3503–3510 (2021).

37. Zhuo, Z. et al. Cycling mechanism of Li_2MnO_3 : $\text{Li}-\text{CO}_2$ batteries and commonality on oxygen redox in cathode materials. *Joule* **5**, 975–997 (2021).
38. Wang, X. et al. Theoretical characterization of X-ray absorption, emission, and photoelectron spectra of nitrogen doped along graphene edges. *J. Phys. Chem. A* **117**, 579–589 (2013).
39. He, M. et al. Concentrated Electrolyte for the Sodium-Oxygen Battery: Solvation Structure and Improved Cycle Life. *Angew. Chem. Int. Ed.* **55**, 15310–15314 (2016).
40. Chen, Y. et al. Steric effect tuned ion solvation enabling stable cycling of high-voltage lithium metal battery. *J. Am. Chem. Soc.* **143**, 18703–18713 (2021).
41. Chang, Z. et al. Beyond the concentrated electrolyte: Further depleting solvent molecules within a Li^+ solvation sheath to stabilize high-energy-density lithium metal batteries. *Energy Environ. Sci.* **13**, 4122–4131 (2020).
42. Burke, C. M. et al. Enhancing electrochemical intermediate solvation through electrolyte anion selection to increase nonaqueous $\text{Li}-\text{O}_2$ battery capacity. *Proc. Nat. Acad. Sci.* **112**, 9293–9298 (2015).
43. Wang, Z. et al. Non-Flammable Ester Electrolyte with Boosted Stability Against Li for High-Performance Li metal Batteries. *Angew. Chem. Int. Ed.* **61**, 202206682 (2022).
44. Sousa da Silva, A. W. & Vranken, W. F. ACPYPE-Antechamber python parser interface. *BMC Res. Notes* **5**, 1–8 (2012).
45. Doherty, B. et al. Revisiting OPLS force field parameters for ionic liquid simulations. *J. Chem. Theory Comput.* **13**, 6131–6145 (2017).
46. Kresse, G. & Furthmüller, J. Efficiency of ab-initio total energy calculations for metals and semiconductors using a plane-wave basis set. *Comp. Mater. Sci.* **6**, 15–50 (1996).
47. Kresse, G. & Furthmüller, J. Efficient iterative schemes for ab initio total-energy calculations using a plane-wave basis set. *Phys. Rev. B.* **54**, 11169 (1996).
48. Blöchl, P. E. Projector augmented-wave method. *Phys. Rev. B.* **50**, 17953 (1994).
49. Kresse, G. & Joubert, D. From ultrasoft pseudopotentials to the projector augmented-wave method. *Phys. Rev. B.* **59**, 1758 (1999).
50. Perdew, J. P., Burke, K. & Ernzerhof, M. Generalized Gradient Approximation Made Simple. *Phys. Rev. Lett.* **77**, 3865 (1996).
51. Yuwono, J. A. et al. Atomistic insights into lithium storage mechanisms in anatase, rutile, and amorphous TiO_2 electrodes. *ACS Appl. Mater. Interfaces* **13**, 1791–1806 (2021).
52. Leung, K. & Tenney, C. M. Toward first principles prediction of voltage dependences of electrolyte/electrolyte interfacial processes in lithium ion batteries. *J. Phys. Chem. C.* **117**, 24224–24235 (2013).
53. Grimme, S., Antony, J., Ehrlich, S. & Krieg, H. A consistent and accurate ab initio parametrization of density functional dispersion correction (DFT-D) for the 94 elements H-Pu. *J. Chem. Phys.* **132**, 154104 (2010).
54. Yan, C. et al. Lithium Nitrate Solvation Chemistry in Carbonate Electrolyte Sustains High-Voltage Lithium Metal Batteries. *Angew. Chem. Int. Ed.* **57**, 14055–14059 (2018).
55. Yamada, Y. et al. Electrochemical lithium intercalation into graphite in dimethyl sulfoxide-based electrolytes: effect of solvation structure of lithium ion. *J. Phys. Chem. C.* **114**, 11680–11685 (2010).
56. Wang, L., Uosaki, K. & Noguchi, H. Effect of electrolyte concentration on the solvation structure of gold/ $\text{LiTFSI}-\text{DMSO}$ solution interface. *J. Phys. Chem. C.* **124**, 12381–12389 (2020).

Acknowledgements

Financial support from the National Natural Science Foundation of China (Grant No. 52104315, W.Z.), the National Key R&D Program of China (No. 2022YFC3900200, W.Z.), and the Australian Research Council (DP210101486 and FL210100050, Z.G.) is acknowledged. Part of this work was carried out at the Soft X-ray (SXR) beamline (beamtime: M18876, G.L.). The authors acknowledge their operational support from ANSTO staff for synchrotron-based characterizations.

Author contributions

F.Z. performed the experiments and wrote the original draft. J.A.Y. performed the theoretical calculations. J.Z. and L.S. performed the catalyst preparation and testing. Y.F. and G.L. conducted part of the cathode characterizations and analysed the data. W.Z. and Z.G. directed the project and revised the manuscript. D.W. provided helpful discussions and English editing.

Competing interests

The authors declare no competing interests.

Additional information

Supplementary information The online version contains supplementary material available at <https://doi.org/10.1038/s41467-024-47629-2>.

Correspondence and requests for materials should be addressed to Wenchao Zhang or Zaiping Guo.

Peer review information *Nature Communications* thanks the anonymous reviewer(s) for their contribution to the peer review of this work. A peer review file is available.

Reprints and permissions information is available at <http://www.nature.com/reprints>

Publisher's note Springer Nature remains neutral with regard to jurisdictional claims in published maps and institutional affiliations.

Open Access This article is licensed under a Creative Commons Attribution 4.0 International License, which permits use, sharing, adaptation, distribution and reproduction in any medium or format, as long as you give appropriate credit to the original author(s) and the source, provide a link to the Creative Commons licence, and indicate if changes were made. The images or other third party material in this article are included in the article's Creative Commons licence, unless indicated otherwise in a credit line to the material. If material is not included in the article's Creative Commons licence and your intended use is not permitted by statutory regulation or exceeds the permitted use, you will need to obtain permission directly from the copyright holder. To view a copy of this licence, visit <http://creativecommons.org/licenses/by/4.0/>.

© The Author(s) 2024